# High Efficient Impedance Tensor Extraction Method for Arbitrarily Shaped Metasurface Elements

Thomas Frey, Aurel Baader, Maximilian Döring, Christian Waldschmidt, Tobias Chaloun



DOI: 10.1109/LAWP.2025.3567324

# High Efficient Impedance Tensor Extraction Method for Arbitrarily Shaped Metasurface Elements

Thomas Frey, *Graduate Student Member, IEEE,* Aurel Baader,
Maximilian Döring, *Graduate Student Member, IEEE,*
Christian Waldschmidt, *Fellow, IEEE,* and Tobias Chaloun, *Senior Member, IEEE*

***Abstract*—Advances in metasurface design have significantly developed high-performance antennas. This work presents a novel method for extracting the anisotropic surface impedance tensor of a pixel geometry within an arbitrarily shaped unit cell. The eigenvectors of the purely isotropic tensor are modified using the rotation matrix to obtain the anisotropic impedance tensor. This creates a 3D-tensor database to assign the analytical impedance tensors to physical pixel geometries. Furthermore, evaluation metrics for anisotropy degree and impedance modulation are introduced to enable a comprehensive metasurface elements characterization. The proposed eigenvector rotation method enables an extremely fast and highly accurate anisotropic tensor extraction and evaluation process. Based on the characterization, an anisotropic holographic-based leaky wave antenna consisting of hexagonal unit cells is fabricated on a fused silica wafer. The far field measurements show a gain of 34.4 dBi, an aperture efficiency of 49 %, polarization purity of 40 dB, and a side-lobe level of 27 dB at 160 GHz.**

***Index Terms*—impedance tensor extraction, anisotropic metasurface, holographic antenna, metasurface antenna.**

## I. Introduction

Holographic-based leaky wave antennas (HLWAs) are based on the interaction of a surface wave (SW) with a periodically modulated surface. This can be implemented by a dense periodic structure of sub-wavelength discontinuities, which physically describes a modulated impedance surface (MIS) [1]–[9]. This MIS hologram provides a highly flexible control in terms of the amplitude and phase of the objective aperture field distribution [4], [10]–[14].
In recently published contributions, a full tensorial synthesis is utilized to assign the analytical impedance tensor to a physical pixel geometry [15]. The impedance tensor extraction of an arbitrary shaped metasurface element is applied by solving a nonlinear system of equations (NLSoE) [15]–[17]. However, an exceedingly detailed eigenmode simulation must be conducted, which renders this method highly time-consuming and necessitates significant computational effort. Furthermore, the NLSoE solution extremely dependents on the input parameters. This leads to inaccuracies of the calculated impedance tensor entries and their corresponding pixel geometry parameters in the 3D-tensor database, which results in an imprecise realization of the MIS hologram.

This work was funded by the German Research Foundation under Grand - CH 2226/4-1. (*Corresponding author: Thomas Frey*)

The authors 1 are with the Institute of Microwave Engineering, Ulm University, 89081 Ulm, Germany e-mail: thomas.frey@uni-ulm.de.

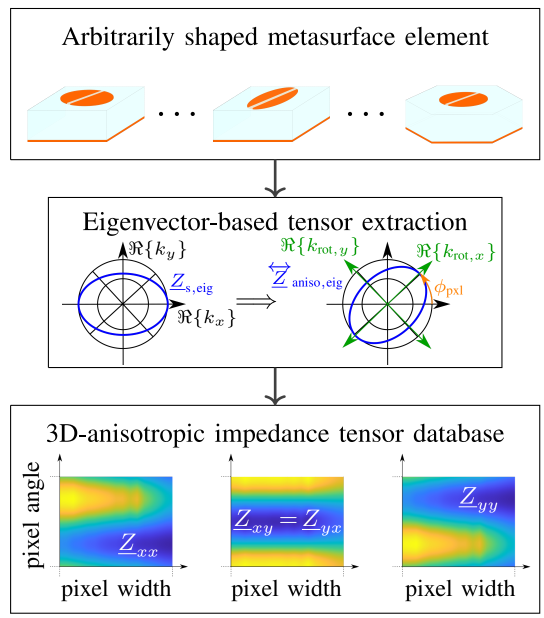


Fig. 1. Illustration of the eigenvector-based tensor extraction method.

In this work, a novel method to extract the impedance tensor of an arbitrary shaped pixel geometry and unit cell (UC) shape is presented. The proposed tensor extraction process entails rotating the eigenvectors (EVs) of a purely isotropic tensor, leading to a modification of those eigenvalues and result in an exceptionally accurate and unambiguous computation of the anisotropic impedance tensor compared to the NLSoE method [15]. This enables an extremely efficient method for extracting and evaluating the anisotropic tensor of arbitrarily shaped metasurface elements. Hence, an even more accurate assignment of the analytical tensor hologram to the corresponding pixel geometries, compared to the NLSoE method, takes place and leads to a significant improvement of the anisotropy degree. A HLWA prototype consisting of hexagonally shaped UCs is realized on a fused silica wafer, encouraged by very high manufacturing accuracy at frequencies above 140 GHz [18].

## II. Impedance Tensor Extraction

To assign the analytical impedance tensor to a physical pixel geometry, a full tensorial synthesis process is employed, as described in [15]. The HFSS Eigenmode solver models an infinitely periodic UC structure with periodic boundary conditions. However, only the computation of the scalar impedance $\underline{Z}s, \text{eig}(\phi\text{inc})$ in possible [19]. Hence, a method to extract the full impedance tensor for arbitrary pixel geometries and UC shapes is needed to generate a 3D-tensor database.

### A. Eigenvector Rotation Method

A novel method to compute the anisotropic impedance tensor of an arbitrary pixel geometry and UC shape using the rotation of the tensor EVs is presented. Since $\phi_{\text{pxl}} = \phi_{\text{inc}}$ applies, no TM/TE-SW coupling occurs and no anisotropic behavior is present. This allows the direct computation of the pure isotropic tensor $\overleftrightarrow{\underline{Z}}_{\text{iso,eig}}$ and its tensor components $\underline{Z}_{xx,\text{eig}}$ and $\underline{Z}_{yy,\text{eig}}$ using the Eigenmode solver by a UC referred incident angle of $\phi_{\text{inc}} = 0°$ for $M$ different pixel widths $w_{\text{pxl},m}$ as follows

$$\underline{Z}_{xx,\text{eig}}\left(w_{\text{pxl},m}\right) = \underline{Z}_{s,\text{eig}}\left(w_{\text{pxl},m},\, \phi_{\text{pxl}} = \phi_{\text{inc}} = 0°\right) , \tag{1}$$

$$\underline{Z}_{yy,\text{eig}}\left(w_{\text{pxl},m}\right) = \underline{Z}_{s,\text{eig}}\left(w_{\text{pxl},m},\, \phi_{\text{pxl}} = 90°,\, \phi_{\text{inc}} = 0°\right) . \tag{2}$$

The EVs of a purely isotropic tensor $\left(\underline{Z}_{xy} = \underline{Z}_{yx} = 0\,\Omega\right)$ are located along the principal axis of the coordinate system in the $\Re\{k_x\}$-$\Re\{k_y\}$-plane. The rotation of those EVs according to the pixel orientation angle $\phi_{\text{pxl}}$ results in a transformation into an anisotropic impedance tensor $\overleftrightarrow{\underline{Z}}_{\text{aniso,eig}}$ (see Fig. 1). Those secondary diagonal corresponds to $\underline{Z}_{xy} \neq 0\,\Omega$ and $\underline{Z}_{yx} \neq 0\,\Omega$ and the anisotropic tensor is calculated to

$$\overleftrightarrow{\underline{Z}}_{\text{aniso,eig}} = \overleftrightarrow{R}\left(\phi_{\text{pxl}}\right) \overleftrightarrow{\underline{Z}}_{\text{iso,eig}} \overleftrightarrow{R}^{-1}\left(\phi_{\text{pxl}}\right) , \tag{3}$$

where the rotation tensor $\overleftrightarrow{R}$ is defined by

$$\overleftrightarrow{R}\left(\phi_{\text{pxl}}\right) = \begin{pmatrix} \cos\left(\phi_{\text{pxl}}\right) & -\sin\left(\phi_{\text{pxl}}\right) \\ \sin\left(\phi_{\text{pxl}}\right) & \cos\left(\phi_{\text{pxl}}\right) \end{pmatrix} . \tag{4}$$

Thus, only the eigenmode simulation of the two isotropic tensor components $\underline{Z}_{xx}$ and $\underline{Z}_{yy}$ across the $M$ pixel width is required, in order to compute the desired $3 \times N \times M$ anisotropic impedance tensor database for $N$ different pixel angles $\phi_{\text{pxl},n}$ as depicted in Fig. 1. This novel EV-based tensor extraction method significantly reduces the calculation effort and results in an even more accurate and unambiguous tensor database solution compared to the NLSoE approach from [15].

### B. Pixel Performance Evaluation Metrics

For the characterization of a desired pixel geometry within an arbitrarily shaped UC, the anisotropy coefficient $\xi$ and the transverse modulation index $M_{\text{t}}$ are introduced. The anisotropy coefficient $\xi$ is calculated as follows

$$\xi = \frac{\left|\underline{Z}_{xy,\text{eig}}\right| + \left|\underline{Z}_{yx,\text{eig}}\right|}{\left|\underline{Z}_{xx,\text{eig}}\right| + \left|\underline{Z}_{yy,\text{eig}}\right| + \left|\underline{Z}_{xy,\text{eig}}\right| + \left|\underline{Z}_{yx,\text{eig}}\right|} \tag{5}$$

and defines the degree of anisotropy of a metasurface element. For a meaningful calculation of $\xi$, the tensor configuration is analyzed to achieve maximum TM/TE SW coupling. In order to evaluate the surface impedance modulation range, the transverse modulation index $\max\left(M_{\text{t}}\right)$ is defined by

$$\max\left(M_{\text{t}}\right) = \frac{\max\left(\underline{Z}_{s,\text{eig,LUT}}\right) - \min\left(\underline{Z}_{s,\text{eig,LUT}}\right)}{\max\left(\underline{Z}_{s,\text{eig,LUT}}\right) + \min\left(\underline{Z}_{s,\text{eig,LUT}}\right)} . \tag{6}$$

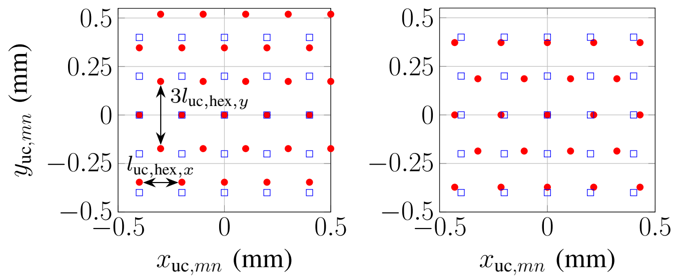


(a) (b)

Fig. 2. Arrangement of hexagonally shaped UCs for a $\varphi_{\text{hex}}$ of 60° (•) and squared shaped UCs (□) on an $1\,\text{mm} \times 1\,\text{mm}$ aperture area (a) equal UC length $l_{\text{uc,hex},x} = l_{\text{uc,square},x}$ (b) equal UC area $A_{\text{uc,hex}} = A_{\text{uc,square}}$.

## III. Hexagonally Shaped Unit Cell Design

In order to obtain a valid eigenmode solution for a hexagonally shaped UC arrangement using periodic boundary conditions, a rectangular cut-out is required [20]. In the following, two different approaches for the implementation of a hexagonally shaped UC compared to the square UC are pursued.

### A. Equal UC dimension in x-direction

In the first hexagonal UC design approach, the UC dimension in $x$-direction is exactly the same as for the square UC. The dimensions and positions of the hexagonal UC arrangement in the $x$-$y$-plane are calculated as presented in [20] (see Fig. 2a)

$$l_{\text{uc,hex},x} = l_{\text{uc,square},x} , \quad l_{\text{uc,hex},y} = \frac{l_{\text{uc,hex},x}}{\sqrt{3}} , \tag{7}$$

$$x_{\text{uc,hex},mn} = l_{\text{uc,hex},x}\left(\left(m + n\,\cos\left(\varphi_{\text{hex}}\right)\right) - \left\lfloor\frac{n}{2}\right\rfloor\right) , \tag{8}$$

$$y_{\text{uc,hex},mn} = n\,l_{\text{uc,hex},x}\sin\left(\varphi_{\text{hex}}\right) \quad \forall m, n \in N_{x,y,\text{hex}} , \tag{9}$$

with $(m, n)$ being the UC number in $x$- and $y$-direction and $\varphi_{\text{hex}}$ equals the hexagon interlock angle. A comparison of a square (□) and hexagonal (•) UC arrangement on an aperture with the $x$- and $y$-dimensions of $1\,\text{mm} \times 1\,\text{mm}$ is depicted in Fig. 2a. The hexagonal shape leads to an interlock of the UCs in $y$-direction which increases the number of UCs $N_{y,\text{hex}}$ by

$$N_{x,\text{hex}} = N_{x,\text{square}} , \quad N_{y,\text{hex}} = \left\lceil \frac{2}{\sqrt{3}} \cdot N_{y,\text{square}} \right\rceil . \tag{10}$$

This leads to an increase of the number of hexagonally shaped UCs by $2/\sqrt{3}$ compared to the square UC arrangement by considering the same aperture area.

### B. Equal UC area

In the second approach, the same area is utilized for the hexagonal UC as for the square UC. The hexagonal UC dimensions in the $x$- and $y$-directions are increased and decreased by exactly the same value

$$l_{\text{uc,hex},x} = \sqrt{\frac{2}{\sqrt{3}}}\, l_{\text{uc,square},x} , \quad l_{\text{uc,hex},y} = \sqrt{\frac{\sqrt{3}}{2}}\, l_{\text{uc,square},x} . \tag{11}$$

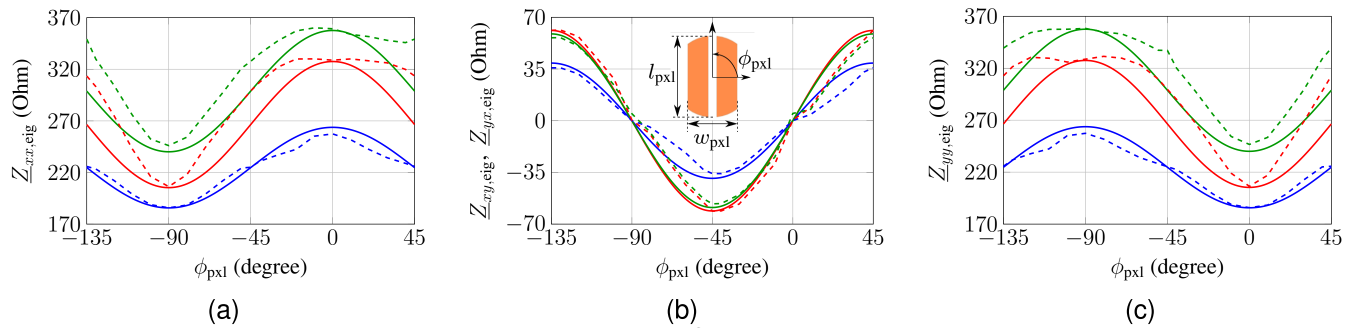


Fig. 3. Eigenmode impedance tensor for a curved rectangular shaped pixel (see ①. in Sec. IV) within the equal length hexagonally shaped UC from Sec. III-A computed by the EV rotation method (solid line) and NLSoE approach (dashed line) for all pixel orientations $\phi_{\text{pxl}} = [-135°, 45°]$ at 160 GHz: (a) $\underline{Z}_{xx,\text{eig}}$, (b) $\underline{Z}_{xy,\text{eig}} = \underline{Z}_{yx,\text{eig}}$, (c) $\underline{Z}_{yy,\text{eig}}$, for the discrete pixel widths $w_{\text{pxl}}$: 40 µm (—), 115 µm (—), 190 µm (—), with a constant pixel length $l_{\text{pxl}} = 190$ µm.

TABLE I
COMPARISON TABLE OF THE PIXEL GEOMETRIES AND UC SHAPES.

| **Parameter** | **UC shape** | **Pixel geometry** ① | ② | ③ | ④ |
|---|---|---|---|---|---|
| **Anisotropy coefficient** (5) | Square | 0.19 | 0.12 | 0.17 | 0.15 |
| | Hex. $l_{\text{uc},x}$ | **0.25** | 0.17 | 0.19 | 0.17 |
| | Hex. $A_{\text{uc}}$ | 0.18 | 0.16 | 0.18 | 0.07 |
| **Maximum mod. index** (6) | Square | 0.28 | 0.27 | 0.27 | 0.29 |
| | Hex. $l_{\text{uc},x}$ | **0.33** | 0.32 | 0.30 | 0.09 |
| | Hex. $A_{\text{uc}}$ | 0.30 | 0.33 | 0.30 | 0.14 |

The UC positions in the $x$-$y$-plane are computed using (8) and (9) with the modified hexagonal UC dimensions from (11). The number of UCs in $x$- and $y$-direction are calculated as follows

$$N_{x,\text{hex}} = \left\lceil \sqrt{\frac{\sqrt{3}}{2}} \cdot N_{x,\text{square}} \right\rceil, \quad N_{y,\text{hex}} = \left\lceil \sqrt{\frac{2}{\sqrt{3}}} \cdot N_{y,\text{square}} \right\rceil. \tag{12}$$

Since the area per UC is equivalent compared to the square shaped UC $A_{\text{uc,hex}} = A_{\text{uc,square}}$, the number of UCs on the aperture remains unchanged. The arrangement of square (□) and hexagonal (•) UCs on an aperture with dimensions of 1 mm × 1 mm is illustrated in Fig. 2b.

## IV. Characterization of Metasurface Elements

The EV rotation method presented in Sec. II-A and the evaluation metrics from Sec. II-B enable an incredibly fast and highly accurate characterization of an arbitrary shaped pixel geometry within a desired UC shape. The following presents four different pixel geometries, which are illustrated in Table I:
① Curved rectangle with slot (CRwS)
② Elliptical pixel with slot (EwS)
③ Elliptical pixel with double slot (EwDS)
④ Diamond pixel with inclined slot (DwS).
The design of the pixel shape was chosen to achieve both, a highly degree of anisotropy (5) and a maximum modulation index (6).

### A. Evaluation of Pixel Geometries and UC Shapes

The impedance tensor extraction method (Sec. II-A) is applied to all pixel geometry and UC shape combinations. A 3D-tensor database is computed for each case, consisting of $M$ pixel widths $w_{\text{pxl},m}$ and $N$ pixel orientation angles $\phi_{\text{pxl},n}$. A comparison of the considered pixel geometry and UC shape combinations is listed in Table I. The CRwS pixel shape (① in Tab. I) in the hexagonal UC having equal $x$-dimension from Sec. III-A exhibits the absolute best behavior in terms of modulation index of 0.33 and highly degree of anisotropy of 0.25 (■ in Tab. I). Its extracted impedance tensor components computed by the EV rotation method from Sec. II-A are shown in Fig. 3 (solid line) for three different pixel widths and a pixel angle range from −135° to 45°. All tensor components exhibit no ripple throughout and an unambiguous progression across the pixel orientation angle (see Fig. 3). The pixel angles 0° and −90° yield an impedance tensor with vanishing anisotropic components, as no electric field couples into the TE component, and the isotropic components exhibit maxima and minima. For $\phi_{\text{pxl}} = \pm 45°$ and −135°, maximum TM/TE surface wave coupling occurs, leading to the maxima in the anisotropic impedance. For a meaningful comparison, the tensor components computed by solving the NLSoE from [15] are depicted in Fig. 3 (dashed line). An erroneous tensor solutions lead to a notable deviation of all the tensor components compared to the EV rotation method, as shown in Fig. 3. The EwS and EwDS pixel (② ③ Tab. I) exhibit acceptable behavior with the EwS pixel acting more anisotropy and the EwDS pixel provides a higher modulation index. Due to its shape, the DwS pixel (④ Tab. I) exhibits an almost purely isotropic tensor and a weak impedance modulation range (■ in Tab. I).

## V. HLWA Realization and Measurement

Based on the metasurface element characterization from Sec. IV, an anisotropic HLWA prototype is realized on a fused silica wafer with a relative permittivity of $\varepsilon_r = 3.78$ and a loss tangent of $\tan\delta = 0.001$. The thickness of the glass wafer is set to 160 µm to suppress higher order SW-modes around the operating frequency of 160 GHz. The circular shaped glass wafer has a diameter of 50.8 mm and the surface wave launcher (SWL) is placed in its

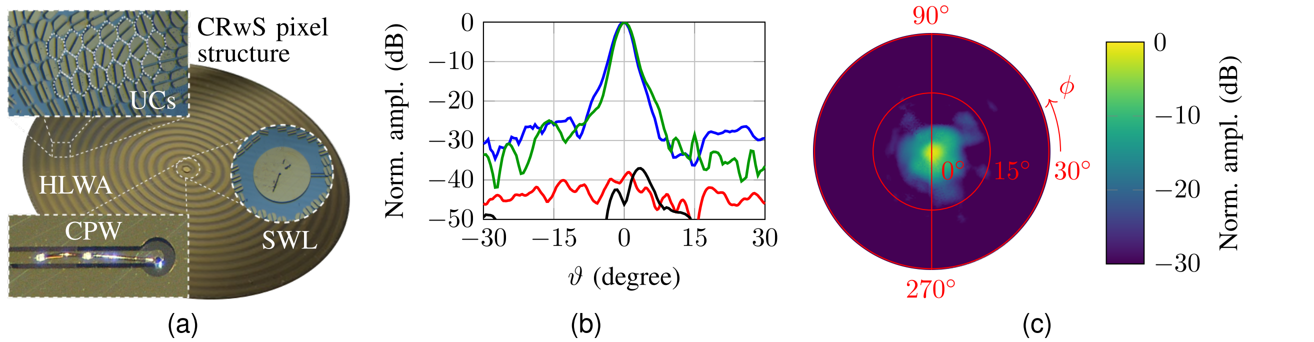


Fig. 4. Measured radiation patterns of the anisotropic HLWA on glass: (a) realized HLWA prototype consisting of hexagonally shaped UCs each with a CRwS pixel in its center, (b) co-pol (— $\phi_0 = 0°$, — $\phi_0 = 90°$) and cross-pol (— $\phi_0 = 0°$, — $\phi_0 = 90°$) at 160 GHz, (c) 3D-co-pol. pattern at 160 GHz.

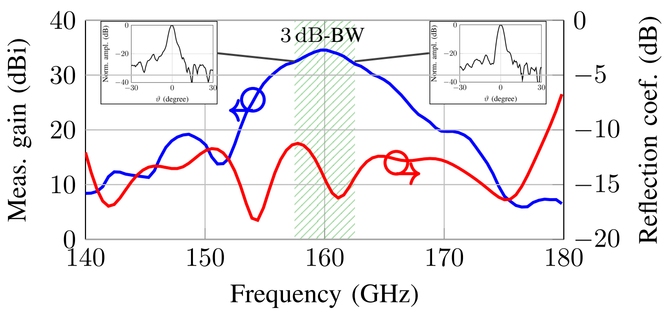


Fig. 5. Measured gain (—) and reflection coefficient (—) from 140 GHz to 180 GHz and measured co-pol (— $\phi_0 = 0°$) at 157.5 GHz and 162.5 GHz.

center at ($x_\mathrm{f} = 0\,\mathrm{mm}, y_\mathrm{f} = 0\,\mathrm{mm}$). A coplanar waveguide (CPW) within the ground metallization in used to excite the HLWA from the bottom side. A bonding wire through the through-glass-via connects the SWL on the upper side of the glass wafer with the CPW line to excite the $\mathrm{TM}_0$ SW mode. The MIS hologram consists of 52 026 hexagonally shaped UCs, as described in Sec. III-A. For the realization of the anisotropic impedance tensors, the pixel geometry is based on a CRwS shaped metal patch (see 1 in Tab. I). The proposed UC configuration provides a maximum impedance variation from j185 Ω to j360 Ω leading to an average impedance of j273 Ω and a maximum transverse modulation index of $\max(M_t) = 0.33$. The HLWA is intended to radiate a right-hand circularly polarized (RHCP) pencil beam under the azimuth and elevation angles ($\vartheta_0 = 0°, \phi_0 = 0°$) at 160 GHz. The metallization of the periodic pixel structure and the ground plane consists of a 10 nm thick chromium seed layer, on which a 350 nm gold layer was sputtered. The individual pixel structures were realized by a conventional wet etching process with tolerances up to ±2 µm. A probe tip in upside-down orientation is used to feed the antenna on glass from the bottom side. The similar measurement setup has been used as described in [21]. The manufactured HLWA prototype on glass is depicted in Fig. 4a. The co-polarization component of the measured 3D-radiation patterns are shown in Fig. 4c for elevation angles up to ±30° and for all azimuth angles. The shape of the main beam, the SLL, and the polarization purity are very well-defined in all azimuth planes. Fig. 4b shows the radiation pattern at the azimuth angles 0° and 90°

TABLE II
COMPARISON TABLE TO THE STATE-OF-THE-ART.

| **Ref.** | **Meas. gain** (dBi) | $f$ (GHz) | **Size** ($\lambda_0^2$) | **SLL** (dB) | **Pol. purity** (dB) | **AE** (%) |
|---|---|---|---|---|---|---|
| This work | 34.4 | 160 | 448 | 27.0 | 40.0 | 49.0 |
| [15] | 32.0 | 160 | 448 | 28.0 | 38.0 | 28.3 |
| [22] | 25.3 | 26 | 54.1 | 18.0 | 20.0 | 49.1 |
| [17] | 26.8 (sim.) | 14 | 100 | 16.0 | - | 38.0 |
| [20] | 34.1 | 162 | 512 | 27.0 | 38.0 | 40.0 |

for an operation frequency of 160 GHz. A minimum SLL of 27 dB and a polarization purity of 40 dB were measured at 160 GHz. The maximum measured antenna gain equals 34.4 dBi and occurs precisely at 160 GHz, corresponding in a notable aperture efficiency (AE) of 49 %. The input reflection coefficient is below −10 dB across the wide frequency range from 140 GHz to 178 GHz, as depicted in Fig. 5. Furthermore, a measured 3 dB-bandwidth (3 dB-BW) regarding the antenna gain of 5 GHz from 157.5 GHz to 162.5 GHz and the corresponding radiation patterns for the azimuth angle 0° can be determined from Fig. 5. The computed directivity based on the measured 3D-radiation pattern is 35.1 dBi, corresponding in a radiation efficiency of at least 85 % within the entire bandwidth of 30 GHz. A comparison with other state-of-the-art HLWA prototypes, is listed in Table II.

## VI. Conclusion

In this letter, a novel method to extract the anisotropic impedance tensor of an arbitrarily shaped metasurface element is presented. For this purpose, the rotation tensor is utilized to modify the eigenvectors of a purely isotropic tensor. This only necessitates the eigenmode simulation of the isotropic components, resulting in a significant reduction in computation time and an even more accurate tensor solution compared to the NLSoE method. For a detailed characterization of the metasurface elements, evaluation metrics are introduced. Based on this characterization process, a HLWA consisting of hexagonal UCs and CRwS pixels is realized on a fused silica wafer, operating at 160 GHz. The measured radiation patterns show a gain of 34.4 dBi, leading to a notable AE of 49 %, a polarization purity of 40 dB and a side-lobe level below 27 dB are achieved.

## Acknowledgment

The authors would like to thank to Norbert Ambrosius from LPKF Laser & Electronics AG for processing and machining the glass wafer to realize the holographic antenna prototype and Heike Frik from the Institute of Microwave Engineering at Ulm University for her technical support in the realization of the HLWA prototype on glass.


## References


[1] G. Minatti, F. Caminita, M. Casaletti, and S. Maci, "Spiral Leaky-Wave Antennas Based on Modulated Surface Impedance," *IEEE Trans. Antennas Propag.*, vol. 59, no. 12, pp. 4436–4444, Dec. 2011.

[2] S. Maci, G. Minatti, M. Casaletti, and M. Bosiljevac, "Metasurfing: Addressing Waves on Impenetrable Metasurfaces," *IEEE Antennas and Wireless Propagation Letters*, vol. 10, pp. 1499–1502, 2011.

[3] G. Minatti, M. Sabbadini, and S. Maci, "Anisotropic surface boundary conditions and their implementations," in *2013 International Symposium on Electromagnetic Theory*, 2013, pp. 660–663.

[4] E. Martini and S. Maci, "Modulated Metasurfaces for Microwave Field Manipulation: Models, Applications, and Design Procedures," *IEEE Journal of Microwaves*, vol. 2, no. 1, pp. 44–56, 2022.

[5] F. Giusti, S. Maci, and E. Martini, "Complete Open-Stopband Suppression Using Sinusoidally Modulated Anisotropic Metasurfaces," *IEEE Transactions on Antennas and Propagation*, vol. 71, no. 11, pp. 8537–8547, 2023.

[6] Y. Sun, B. Cai, L. Yang, L. Wu, Y. Cheng, H. Luo, F. Chen, and X. Li, "High-Gain Dual-Polarization Microstrip Antenna Based on Transmission Focusing Metasurface," *Materials*, vol. 17, no. 15, 2024. [Online]. Available: https://www.mdpi.com/1996-1944/17/15/3730

[7] H. Liu, Y. Cheng, H. Luo, F. Chen, L. Yang, and X. Li, "Reconfigurable Microstrip Bandpass Filter Based on Spoof Surface Plasmon Polaritons of M-Cusp-H-Type Cells," *IEEE Transactions on Circuits and Systems II: Express Briefs*, vol. 71, no. 6, pp. 3031–3035, 2024.

[8] W. Tian, L. Yang, B. Cai, Y. Cheng, F. Chen, H. Luo, and X. Li, "Design and Analysis of Dual-Band Metasurface Filter for Pulse Waves Based on Capacitive Nonlinear Circuits," *Electronics*, vol. 14, no. 3, 2025. [Online]. Available: https://www.mdpi.com/2079-9292/14/3/603

[9] Y. Sun, L. Yang, J. Wang, Y. Cheng, H. Luo, F. Chen, and X. Li, "Microstrip antenna loaded with focusing metasurface for high-gain dual-polarization and bidirectional radiation," *Journal of Applied Physics*, vol. 137, no. 1, p. 013104, 01 2025. [Online]. Available: https://doi.org/10.1063/5.0243559

[10] G. Minatti, M. Faenzi, E. Martini, F. Caminita, P. D. Vita, D. González-Ovejero, M. Sabbadini, and S. Maci, "Modulated Metasurface Antennas for Space: Synthesis, Analysis and Realizations," *IEEE Trans. Antennas Propag.*, vol. 63, no. 4, pp. 1288–1300, Apr. 2015.

[11] G. Minatti, F. Caminita, E. Martini, M. Sabbadini, and S. Maci, "Synthesis of Modulated-Metasurface Antennas With Amplitude, Phase, and Polarization Control," *IEEE Transactions on Antennas and Propagation*, vol. 64, no. 9, pp. 3907–3919, 2016.

[12] G. Minatti, F. Caminita, E. Martini, and S. Maci, "Flat Optics for Leaky-Waves on Modulated Metasurfaces: Adiabatic Floquet-Wave Analysis," *IEEE Trans. Antennas Propag.*, vol. 64, no. 9, pp. 3896–3906, 2016.

[13] M. Faenzi, D. González-Ovejero, and S. Maci, "Wideband Active Region Metasurface Antennas," *IEEE Transactions on Antennas and Propagation*, vol. 68, no. 3, pp. 1261–1272, 2020.

[14] ——, "Flat Gain Broadband Metasurface Antennas," *IEEE Transactions on Antennas and Propagation*, vol. 69, no. 4, pp. 1942–1951, 2021.

[15] T. Frey, M. Döring, C. Waldschmidt, and T. Chaloun, "A Full Tensorial Synthesis Method for Holographic-Based Leaky Wave Antennas," *IEEE Antennas Wireless Propag. Lett.*, pp. 1–5, 2023.

[16] B. H. Fong, J. S. Colburn, J. J. Ottusch, J. L. Visher, and D. F. Sievenpiper, "Scalar and Tensor Holographic Artificial Impedance Surfaces," *IEEE Transactions on Antennas and Propagation*, vol. 58, no. 10, pp. 3212–3221, Oct. 2010.

[17] Y. Wen, P.-Y. Qin, S. Maci, and Y. J. Guo, "Low-Profile Multibeam Antenna Based on Modulated Metasurface," *IEEE Transactions on Antennas and Propagation*, vol. 71, no. 8, pp. 6568–6578, 2023.

[18] T. Chaloun, S. Brandl, N. Ambrosius, K. Kröhnert, H. Maune, and C. Waldschmidt, "RF Glass Technology Is Going Mainstream: Review and Future Applications," *IEEE Journal of Microwaves*, vol. 3, no. 2, pp. 783–799, 2023.

[19] HFSS version 23.1, Ansys Cooperation, Canonsburg, PA, USA, 2023.

[20] T. Frey, A. Baader, M. Döring, C. Waldschmidt, and T. Chaloun, "A Hexagonally Shaped Unit Cell for Holographic-Based Leaky Wave Antennas," in *2024 International Symposium on Antennas and Propagation (ISAP)*, 2024, pp. 1–2.

[21] T. Galler, T. Frey, C. Waldschmidt, and T. Chaloun, "High-Gain Millimeter-Wave Holographic Antenna in Package using Glass Technology," *IEEE Antennas Wireless Propag. Lett.*, pp. 1–5, 2020.

[22] S. Xue, Y. Shen, Z. Xu, W. Wan, and S. Hu, "Double-Layer Cross-Embedded Holographic Antennas With Compact Size and High Efficiency," *IEEE Transactions on Antennas and Propagation*, vol. 72, no. 7, pp. 5436–5446, 2024.